











## PAPER

[View Article Online](#)  
[View Journal](#) | [View Issue](#)Cite this: *Dalton Trans.*, 2025, **54**, 11193Selective synthesis of  $\beta$ -TaON: The critical influence of oxygen partial pressure in ammonolysis†Mirabbos Hojamberdiev, <sup>a,b</sup> Ronald Vargas, <sup>c,d</sup> Lorean Madriz, <sup>c,d</sup> Dilshod Nematov, <sup>e,f</sup> Ulugbek Shaislamov, <sup>g</sup> Hajime Wagata, <sup>h</sup> Yuta Kubota, <sup>b</sup> Kunio Yubuta, <sup>i</sup> Katsuya Teshima <sup>i</sup> and Nobuhiro Matsushita <sup>b</sup>

Tantalum oxynitride (TaON), a member of the transition metal oxynitride family, shows strong potential for solar water splitting due to its tunable optoelectronic properties and visible-light absorption. However, the selective synthesis of thermodynamically stable  $\beta$ -TaON with high phase purity remains challenging because of competing phase formation and sensitivity to processing conditions. In this study, we demonstrate a systematic approach to synthesizing  $\beta$ -TaON by precisely controlling the oxygen partial pressure during the ammonolysis of  $\text{Ta}_2\text{O}_5$ . The oxygen partial pressure is found to critically govern the sequential phase transformation from  $\text{Ta}_2\text{O}_5$  to  $\text{Ta}_3\text{N}_5$ , with  $0.25 \text{ L h}^{-1}$  delineating the narrow synthesis window required for obtaining phase-pure  $\beta$ -TaON. Comprehensive structural, morphological, optical, and chemical characterizations, complemented by density functional theory (DFT) calculations, reveal strong correlations between nitrogen incorporation, band structure modulation, light absorption, and charge transport properties. Photoelectrochemical (PEC) measurements under simulated solar illumination present that mixed-phase  $\beta$ -TaON/ $\text{Ta}_3\text{N}_5$  heterostructures exhibit significantly enhanced photocurrent densities, the possibility of operation at higher power densities, and a favorable band alignment conducive to efficient water oxidation due to enhanced light absorption, effective spatial separation of charge carriers, and improved interfacial charge transfer. The introduction of a sacrificial electron donor further enhances PEC performance by promoting interfacial charge transfer and suppressing charge carrier recombination. These findings establish oxygen partial pressure as a critical synthesis parameter for controlling phase composition and tuning the optoelectronic properties of tantalum (oxy)nitrides, offering a promising strategy for the development of high-performance photoanodes for solar fuel production.

Received 20th May 2025,  
Accepted 21st June 2025

DOI: 10.1039/d5dt01193k

[rsc.li/dalton](https://rsc.li/dalton)

## 1. Introduction

Mixed-anion solid-state compounds are an emerging class of materials with new functions for designing heterogeneous photocatalysts for solar water splitting.<sup>1,2</sup> Among them, tran-

sition metal oxynitrides have attracted significant interest due to their tunable electronic structures, optimal band gaps for visible-light absorption, and favorable conduction and valence band positions, which enable efficient charge carrier separation and redox reactions.<sup>3,4</sup> As a member of the transition

<sup>a</sup>Mads Clausen Institute, University of Southern Denmark, Alsion 2, 6400 Sønderborg, Denmark<sup>b</sup>Department of Materials Science and Engineering, School of Materials and Chemical Technology, Institute of Science Tokyo, 2-12-1 Ookayama, Meguro, Tokyo 152-8550, Japan. E-mail: mirabbos@mci.sdu.dk<sup>c</sup>Instituto Tecnológico de Chascomús (INTECH), Consejo Nacional de Investigaciones Científicas y Técnicas (CONICET), Universidad Nacional de San Martín (UNSAM), Avenida Intendente Marino, Km 8, 2, B7130IWA Chascomús, Provincia de Buenos Aires, Argentina<sup>d</sup>Escuela de Bio y Nanotecnologías, Universidad Nacional de San Martín (UNSAM), Avenida Intendente Marino, Km 8, 2, B7130IWA Chascomús, Provincia de Buenos Aires, Argentina<sup>e</sup>Physical-Technical Institute, National Academy of Sciences of Tajikistan, Dushanbe 734063, Tajikistan<sup>f</sup>School of Optoelectronic Engineering & CQUPT-BUL Innovation Institute, Chongqing University of Posts and Telecommunications, Chongqing 400065, China<sup>g</sup>Center for Development of Nanotechnology at the National University of Uzbekistan, University Str. 4, 100174 Tashkent, Uzbekistan<sup>h</sup>Department of Applied Chemistry, School of Science and Technology, Meiji University, 1-1-1-D615 Higashimita, Tama, Kawasaki 214-8571, Japan<sup>i</sup>Institute for Aqua Regeneration, Shinshu University, 4-17-1 Wakasato, Nagano 380-8553, Japan† Electronic supplementary information (ESI) available. See DOI: <https://doi.org/10.1039/d5dt01193k>

metal oxynitride family, tantalum oxynitride (TaON) has garnered particular attention for its potential applications in solar water splitting. To date, stable and metastable polymorphs of TaON have been reported. The thermodynamically most stable polymorph of TaON is the  $\beta$ -phase, which was first synthesized by Brauer and Weidlein.<sup>5</sup>  $\beta$ -TaON adopts a monoclinic baddeleyite-type structure with space group  $P2_1/c$ , as previously reported for isostructural  $ZrO_2$ , exhibits a bright yellow color, and has direct and indirect optical band gaps of 2.74 eV and 2.37 eV, respectively.<sup>6</sup> Its metastable polymorph ( $\gamma$ -TaON) was synthesized by Schilling *et al.*<sup>7</sup> and reported to crystallize in the monoclinic  $VO_2(B)$ -type structure with space group  $C2/m$ , exhibits an orange color,<sup>8,9</sup> and has direct and indirect optical band gaps of 2.59 eV and 2.03 eV, respectively.<sup>6</sup> An ordered arrangement of oxygen and nitrogen for both  $\beta$ - and  $\gamma$ -TaON crystal structures was reported.<sup>7,10</sup> Another metastable polymorph  $\delta$ -TaON, with a tetragonal anatase-type structure with space group  $I4_1/amd$ , was successfully synthesized by Lüttke *et al.*,<sup>11</sup> which transforms to stable baddeleyite-type  $\beta$ -TaON at elevated temperatures. Earlier studies have also revealed the formation of anatase-type phases by partial substitution of lower-valent cations, such as  $Mg^{2+}$  or  $Sc^{3+}$ , for  $Ta^{5+}$  in TaON.<sup>12,13</sup> Buslaev *et al.*<sup>14</sup> previously proposed the existence of a hexagonal polymorph  $\alpha$ -TaON, which has since been refuted based on quantum-chemical calculations.<sup>15</sup> The high-pressure experiments conducted up to 70 GPa (at ambient temperature)<sup>16</sup> confirmed a pressure-induced transformation from a monoclinic baddeleyite-structured  $\beta$ -TaON into an orthorhombic cotunnite-structured polymorph with space group  $Pnma$  in the 30–35 GPa range.

Despite the structural richness of TaON polymorphs, the  $\beta$ -phase remains the most intensively investigated due to its thermodynamic stability and promising photocatalytic activity. However, its synthesis is often complicated by competing phase formation, stoichiometric deviations, and defect generation during ammonolysis. Among the various polymorphs,  $\beta$ -TaON has been intensively explored for solar water splitting. Although a quantum yield of 10% for photocatalytic  $O_2$  evolution has already been reported for  $\beta$ -TaON,<sup>17</sup> synthesizing  $\beta$ -TaON with high phase purity, an optimal N : O stoichiometry, and well-defined morphology<sup>18,19</sup> remains challenging, requiring precise control over key parameters, such as reaction temperature, reaction time, nitrogen source, *etc.* Especially, conventional synthesis methods often result in the formation of  $Ta_3N_5$  due to the relatively low thermodynamic stability of  $\beta$ -TaON, which can adversely impact its performance. To suppress the formation of  $Ta_3N_5$  during the synthesis of  $\beta$ -TaON, Orhan *et al.*<sup>20</sup> employed a moisturized ammonia atmosphere, generated by passing the commercial ammonia gas through water prior to its introduction into the reaction furnace. Rohloff *et al.*<sup>21</sup> studied the role of synthesis conditions on structural defects and lattice strain in  $\beta$ -TaON using a mixture of ammonia and oxygen, and revealed that the heavily anisotropically microstrained  $\beta$ -TaON was less effective in photochemical and photoelectrochemical water oxidation in comparison to the unstrained one, due to the lattice defects acting as

charge carrier traps.<sup>22</sup> Yoon *et al.*<sup>23</sup> studied the influence of the ammonolysis temperature (800–1000 °C) of  $Ta_2O_5$  on the photocatalytic activity of  $\beta$ -TaON and achieved the highest oxygen evolution rate of 220  $\mu\text{mol g}^{-1} \text{h}^{-1}$  for  $\beta$ -TaON synthesized at 800 °C. Recently, Kodera and Sayama<sup>24</sup> investigated the degree of nitridation of  $Ta_2O_5$  to  $\beta$ -TaON by quantitatively analyzing the change in the weight of a powder after nitridation and identified three regions. They found that although XRD patterns indicated phase-pure  $\beta$ -TaON, the sample nitrided for the initial 1 h exhibited a higher oxygen evolution activity of 250  $\mu\text{mol h}^{-1}$  compared to the sample nitrided for 15 h. This indicates that careful optimization of the nitridation process plays a crucial role in enhancing the photocatalytic efficiency of  $\beta$ -TaON.

In this study, we report a systematic approach to synthesizing phase-pure  $\beta$ -TaON by precisely controlling the oxygen partial pressure ( $p_{O_2}$ ), which was varied by adjusting the  $O_2$  flow rate from 0 to 0.35  $\text{L h}^{-1}$ , during the ammonolysis of  $Ta_2O_5$ . The phase transitions from tantalum oxide to oxide nitride and from tantalum oxide nitride to tantalum nitride were thoroughly investigated to assess their influence on phase purity, crystallinity, particle morphology, size distribution, optical properties, and photoelectrochemical performance. Density functional theory (DFT) calculations were employed to elucidate the electronic structures, density of states, and carrier effective masses, revealing correlations between structural and electronic properties and photoredox performance. In addition to structural and optical characterization, photoelectrochemical (PEC) measurements were conducted under solar irradiation to assess the charge carrier dynamics of the synthesized materials. To better probe surface-related processes and overcome potential limitations in water oxidation activity, a sacrificial electron donor (SED) was employed. The photocurrent–potential behavior and the variation of open-circuit potential (OCP) with irradiance provided insight into the balance between charge transfer and recombination processes. These measurements highlight the role of oxygen partial pressure during synthesis in determining the photoelectrochemical response of tantalum (oxy)nitrides. The findings of this study offer a pathway for optimizing the synthesis of tantalum oxide nitride and tantalum nitride for energy conversion applications.

## 2. Experimental

### 2.1. Synthesis

Tantalum pentoxide ( $Ta_2O_5$ , 0.15 g, 99%, Alfa Aesar) was placed in a corundum crucible and subjected to ammonolysis in a horizontal tube furnace (Carbolite Gero®) equipped with a  $SiO_2$  tube under a localized gas delivery system.<sup>25</sup> The sample was heated up to 900 °C at a heating rate of 400  $\text{K h}^{-1}$  and held at this temperature for 12 h in a mixed atmosphere of ammonia ( $NH_3$ , 10  $\text{L h}^{-1}$ ,  $\geq 99.95\%$ , air liquide) and oxygen ( $O_2$ , 99.999%, air liquide). **CAUTION! Ammonia is a toxic, corrosive, and flammable gas that can cause severe skin burns, eye**

damage, and respiratory irritation (H221, H314, H331). It must be handled only in well-ventilated areas using appropriate conditions and personal protective equipment (P220, P260, P280), and exposure to vapors must be avoided (P261). In case of contact with the eyes or skin, it must be rinsed immediately with water and medical attention must be sought (P303, P305, P312, P338, P351, P353, P361). In case of inhalation, immediate removal to fresh air is necessary (P304, P340), and the leak must be stopped if safe to do so (P376). Oxygen is a non-flammable gas but supports and accelerates the combustion of other materials, causing fire (H270), and pressurized oxygen may explode if heated (H280). It must be handled away from combustible materials under appropriate conditions (P220), valves and fittings must be free from oil and grease (P244), and in case of fire, the leak must be stopped if safe to do so (P370 and P376). After the high-temperature reaction, the sample was allowed to cool naturally to room temperature. The ammonolysis process was conducted under varying oxygen partial pressure ( $p_{O_2}$ ) by adjusting the  $O_2$  flow rate from 0 to 0.05, 0.15, 0.25, and 0.35 L h<sup>-1</sup>, while maintaining the  $NH_3$  flow rate at 10 L h<sup>-1</sup>. According to the oxygen flow rate, the resulting samples were designated as 0-O2, 0.05-O2, 0.15-O2, 0.25-O2, and 0.35-O2, along with Ta<sub>2</sub>O<sub>5</sub>.

## 2.2. Characterization

X-ray diffraction (XRD) patterns were obtained using a PANalytical X'Pert Pro powder diffractometer operated with nickel-filtered Cu-K $\alpha$  radiation at 40 kV and 30 mA. The powder diffraction data were collected in a Bragg–Brentano setup with a  $\theta/\theta$ -arrangement at ambient temperature over an angular range of  $2\theta = 10$ – $80^\circ$  with a step size of  $0.020^\circ$ . The microstructure of the samples was examined using a scanning electron microscope (SEM; Zeiss Gemini 982, Carl Zeiss) at an operating voltage of 5 kV. The nanostructures of the samples were characterized using a transmission electron microscope (TEM; EM-002B, TOPCON) with an accelerating voltage of 160 kV. In each sample, multiple regions were analyzed by SEM and TEM to ensure reproducibility, with representative images chosen from a consistently observed set of morphologies, structural features, porosity, and particle sizes. The surface chemical states of the samples were analyzed by X-ray photoelectron spectroscopy (XPS, JPS-9010MX, JEOL) using Mg-K $\alpha$  radiation.

The ultraviolet-visible (UV-Vis) diffuse reflectance spectra of the samples were measured using an Evolution 220 UV-vis spectrometer (Thermo Fisher Scientific).

## 2.3. Photoelectrochemical (PEC) performance test

Photoelectrochemical (PEC) characterization was performed to investigate the light-induced charge transfer behavior of photocatalyst powders immobilized on the electron-collecting electrode surfaces. The PEC experiments were carried out using a Metrohm-DropSens  $\mu$ STAT200 potentiostat. A 100  $\mu$ L volume of electrolyte was used, with an illuminated geometric area of 0.13 cm<sup>2</sup>. Screen-printed electrodes (DropSens 110) served as the conductive substrate for the photocatalyst, which was immobilized by dip-coating, following a procedure analogous to that reported elsewhere.<sup>26</sup> Briefly, a suspension was pre-

pared by dispersing the photocatalyst powder at a concentration of 1.0 mg mL<sup>-1</sup> in an ethanol/water (1:1) mixture, followed by ultrasonication for 30 min. The resulting suspension was deposited onto the electrode surface, covered with a glass beaker, and dried using a heat gun at 80 °C for 10 min. This procedure was repeated consecutively three times, typically reaching a mass loading around 0.18 mg cm<sup>-2</sup>. The PEC measurements were conducted in 0.1 M Na<sub>2</sub>SO<sub>4</sub> electrolyte, which was deaerated by N<sub>2</sub> bubbling for 10 min. Illumination was provided using simulated solar light (290–900 nm) with an intensity of approximately 100 mW cm<sup>-2</sup> (Solar Light Co.). In the photoelectrochemical cell, a carbon ring was employed as the counter electrode (concentric with the working electrode) and an Ag/AgCl electrode as the reference electrode. All measured potentials were converted to the reversible hydrogen electrode (RHE) scale using the Nernst equation:

$$E \text{ (vs. RHE)} = E \text{ (vs. Ag/AgCl)} + 0.059 \times \text{pH} + 0.197 \quad (1)$$

Linear sweep voltammetry (LSV) was conducted at a scan rate of 10 mV s<sup>-1</sup>. The photoelectrochemical power density ( $P$ ) was estimated from the photocurrent response using the equation:

$$P = J \times (E_0 - E) \quad (2)$$

where  $J$  is the photocurrent density,  $E_0$  is the standard oxidation potential of water, and  $E$  is the applied potential.<sup>27,28</sup> The open-circuit potential (OCP) of each coated electrode was monitored using a PalmSens4 potentiostat as a function of incident light intensity (30, 50, 80, 100, and 150 mW cm<sup>-2</sup>). In addition, chronoamperometry (CA) was conducted at 1 V vs. RHE under chopped light conditions, first in the presence of the supporting electrolyte alone, and subsequently after the addition of 5 mM potassium ferrocyanide.

## 2.4. Density functional theory (DFT) calculations

Quantum-chemical calculations in the framework of density functional theory (DFT) were performed using the Vienna *ab initio* simulation package (VASP).<sup>29</sup> The interaction between valence electrons and ionic cores was described using the project augmented wave (PAW) method. A plane-wave cutoff energy of 800 eV was employed to ensure accurate representation of the wave functions. In contrast to previous DFT studies on tantalum-based oxides and (oxy)nitriles, which often employed standard functionals such as PBE or GGA + U,<sup>30,31</sup> the present work adopts the strongly constrained and appropriately normed (SCAN) meta-GGA functional.<sup>32</sup> SCAN offers improved accuracy in geometry optimization and a more reliable description of the ground-state properties of the complex systems. To achieve more accurate predictions of band gaps and optoelectronic properties, the hybrid HSE06 functional<sup>33</sup> was also employed. HSE06 is well-known for its high accuracy in predicting the electronic properties of a wide variety of materials.<sup>33–35</sup> While several previous studies have computationally explored the properties of tantalum-based oxide and (oxy)nitriles,<sup>30,31,36–39</sup> the use of SCAN and HSE06

functionals – or their combination – remains largely unexplored, with the exception of a couple of studies focused specifically on  $\beta$ -TaON.<sup>38,39</sup> In contrast to earlier works, this study presents a comprehensive analysis of the electronic structures, effective charge carrier masses, and optical properties of Ta<sub>2</sub>O<sub>5</sub>,  $\beta$ -TaON, and Ta<sub>3</sub>N<sub>5</sub>. This systematic approach not only enhances the understanding of the electronic behaviors of each compound but also allows the identification of general trends and key differences in these compounds. The exchange–correlation energy within the HSE06 functional is calculated according to the following expression:

$$E_{xc}^{HSE} = \alpha E_{xc}^{HF,SR}(\omega) + (1 - \alpha) E_{xc}^{PBE,SR}(\omega) + E_{xc}^{PBE,LR}(\omega) + E_{xc}^{PBE} \quad (3)$$

where  $\omega$  is the adjustable parameter governing the extent of short-range interactions, and  $\alpha$  is the fraction of Hartree–Fock (HF) exchange. The hybrid functional ( $E_{xc}^{HSE}$ ) is equivalent to PBE0<sup>40</sup> for  $\omega = 0$  and asymptotically reaches the popular PBE for  $\omega \rightarrow 0$ .

Following the calculation of the electronic structures of the studied materials, the effective masses of charge carriers were estimated. These values were easily derived from the curvature of the electronic bands, which corresponds to the second derivative of the energy with respect to the wave vector. The effective masses for holes and electrons were calculated using the equation:

$$m_{h(e)}^* = \frac{\hbar^2}{d^2 E_{v(c)}/dk^2} \quad (4)$$

where  $m_{h(e)}^*$  denotes holes (h) and electrons (e), and  $E_v$  and  $E_c$  correspond to the energy at the valence band maximum and conduction band minimum, respectively.

### 3. Results and discussion

Fig. 1 shows the X-ray diffraction (XRD) patterns of the as-received Ta<sub>2</sub>O<sub>5</sub> and 0.35-O<sub>2</sub>, 0.25-O<sub>2</sub>, 0.15-O<sub>2</sub>, 0.05-O<sub>2</sub>, and 0-O<sub>2</sub> samples synthesized under varying oxygen partial pressures ( $p_{O_2}$ ) of 0.35, 0.25, 0.15, 0.05, and 0 L h<sup>−1</sup>, respectively. In Fig. 1a, the XRD pattern of the as-received sample shows reflections characteristic of orthorhombic Ta<sub>2</sub>O<sub>5</sub> (ICDD PDF Card No. 98-004-3498) with space group *Amm*2 (no. 38). When  $p_{O_2}$  is set to 0.35 L h<sup>−1</sup>, additional reflections attributed to monoclinic  $\beta$ -TaON (ICDD PDF Card No. 98-000-2363) with space group *P2*<sub>1</sub>/*c* (no. 14) start to emerge, while the reflections belonging to Ta<sub>2</sub>O<sub>5</sub> remain dominant. This indicates the onset of nitrogen incorporation into the Ta<sub>2</sub>O<sub>5</sub> lattice, forming the  $\beta$ -TaON phase. At  $p_{O_2} = 0.25$  L h<sup>−1</sup>, a more pronounced phase transformation occurs. The reflections of Ta<sub>2</sub>O<sub>5</sub> completely disappear, and those corresponding to  $\beta$ -TaON become predominant, indicating the successful formation of phase-pure  $\beta$ -TaON. Further reduction of  $p_{O_2}$  to 0.15 L h<sup>−1</sup> still favors the formation of  $\beta$ -TaON. However, insignificant peak broadening may suggest the beginning of structural change or the potential emergence of a nitrogen-rich secondary phase. At  $p_{O_2} =$

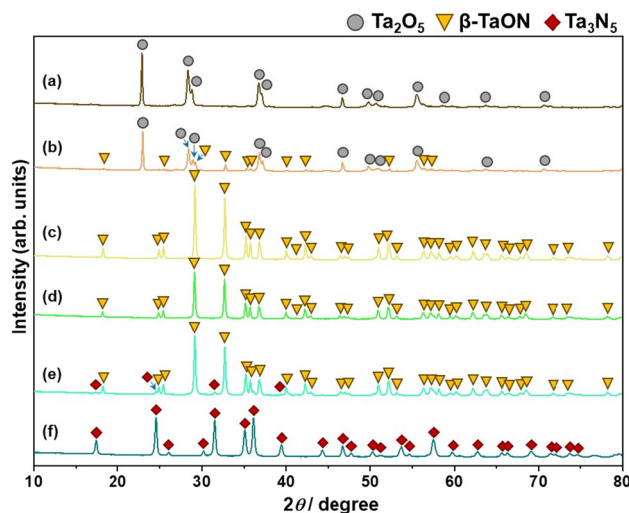


Fig. 1 XRD patterns of the as-received Ta<sub>2</sub>O<sub>5</sub> (a) and 0.35-O<sub>2</sub> (b), 0.25-O<sub>2</sub> (c), 0.15-O<sub>2</sub> (d), 0.05-O<sub>2</sub> (e), and 0-O<sub>2</sub> (f) samples synthesized under oxygen partial pressures ( $p_{O_2}$ ) of 0.35, 0.25, 0.15, 0.05, and 0 L h<sup>−1</sup>, respectively.

0.05 L h<sup>−1</sup>, this trend becomes more pronounced, and low-intensity reflections corresponding to orthorhombic Ta<sub>3</sub>N<sub>5</sub> (ICDD PDF Card No. 98-006-6533) with space group *Cmcm* (no. 63) appear alongside those of  $\beta$ -TaON, implying that the oxygen supply is insufficient to stabilize  $\beta$ -TaON as a single phase.

Finally, at  $p_{O_2} = 0$  L h<sup>−1</sup>, the XRD pattern exhibits intense and well-defined reflections solely attributable to Ta<sub>3</sub>N<sub>5</sub>, confirming the complete transformation to this nitrogen-rich phase in the absence of oxygen. The XRD results present a systematic phase transformation pathway governed by  $p_{O_2}$  under the applied synthesis conditions:



Among different oxygen partial pressures,  $p_{O_2} = 0.25$  L h<sup>−1</sup> was found to be favorable to synthesize phase-pure  $\beta$ -TaON, which acts as an important intermediate during phase transformation from Ta<sub>2</sub>O<sub>5</sub> to Ta<sub>3</sub>N<sub>5</sub>. This tunable phase transformation pathway is pivotal for tailoring the optoelectronic and catalytic properties of tantalum-based materials. Furthermore, it offers a viable one-step synthesis route for synthesizing Ta<sub>2</sub>O<sub>5</sub>/ $\beta$ -TaON and  $\beta$ -TaON/Ta<sub>3</sub>N<sub>5</sub> composites with potential applications in energy conversion.

Fig. 2 shows the scanning electron microscopy (SEM) images of the as-received Ta<sub>2</sub>O<sub>5</sub> and 0.35-O<sub>2</sub>, 0.25-O<sub>2</sub>, 0.15-O<sub>2</sub>, 0.05-O<sub>2</sub>, and 0-O<sub>2</sub> samples synthesized under varying oxygen partial pressures ( $p_{O_2}$ ) of 0.35, 0.25, 0.15, 0.05, and 0 L h<sup>−1</sup>, respectively. In Fig. 2a, the as-received Ta<sub>2</sub>O<sub>5</sub> exhibits agglomerated large particles with sizes ranging from approximately 100–300 nm. The particles possess well-defined boundaries and a relatively porous structure, indicative of loosely packed morphology. When  $p_{O_2}$  is set to 0.35 L h<sup>−1</sup>, the microstructure gradually transforms into a highly porous and sponge-like



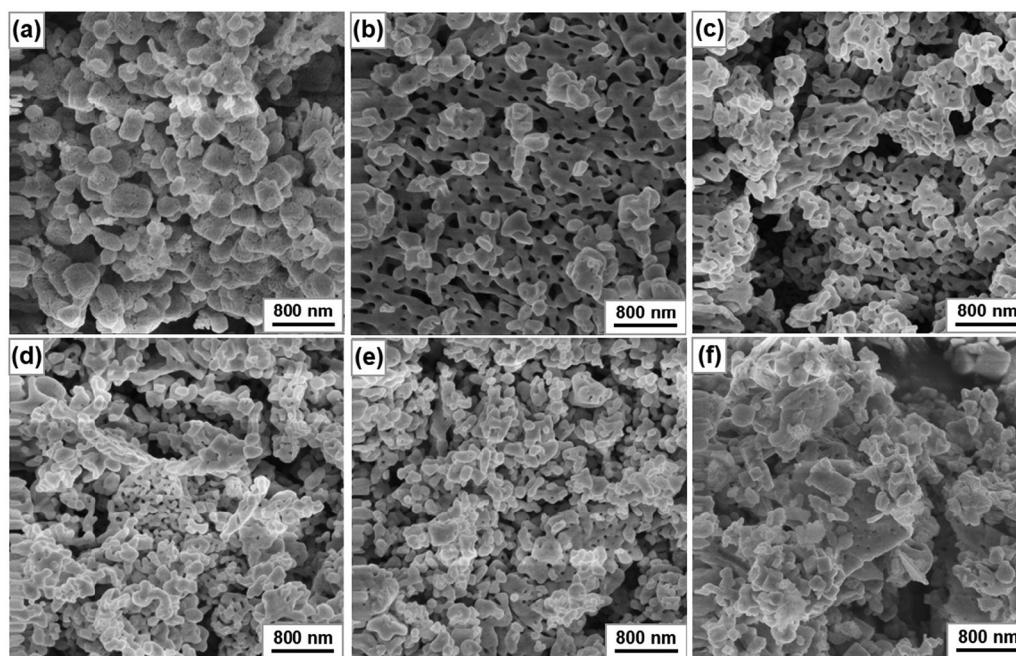


**Fig. 2** SEM images of the as-received  $\text{Ta}_2\text{O}_5$  (a) and 0.35-O2 (b), 0.25-O2 (c), 0.15-O2 (d), 0.05-O2 (e), and 0-O2 (f) samples synthesized under oxygen partial pressures ( $p_{\text{O}_2}$ ) of 0.35, 0.25, 0.15, 0.05, and 0  $\text{L h}^{-1}$ , respectively.

network composed of fine, interconnected crystals, revealing the onset of the lattice condensation process caused by the partial substitution of  $\text{O}^{2-}$  with  $\text{N}^{3-}$  in the anion network (Fig. 2b).<sup>41,42</sup> A similar phenomenon was previously reported by Hojamberdiev *et al.*<sup>18,43,44</sup> for oxynitride systems, where anion substitution led to significant morphological and structural modifications. The reduction in  $p_{\text{O}_2}$  to 0.25  $\text{L h}^{-1}$  maintains the overall sponge-like network with a noticeable decrease in pore size (Fig. 2c). At  $p_{\text{O}_2} = 0.15 \text{ L h}^{-1}$ , the number of pores gradually diminishes, and irregularly shaped and denser particles begin to form (Fig. 2d). Denser particles with an average size of 100–200 nm are formed on the surface of larger porous particles at  $p_{\text{O}_2} = 0.05 \text{ L h}^{-1}$ , while the number of pores continues to decrease, implying surface reconstruction (Fig. 2e). Finally,  $p_{\text{O}_2} = 0 \text{ L h}^{-1}$ , the sample shows densely packed morphology with irregular particles with an average size of 150–250 nm and a limited porosity. Some particle surfaces also feature regions with poorly defined outlines and indistinct textural contrasts, which may be associated with an amorphous or low crystalline nature (Fig. 2f). The SEM results indicate that phase-pure  $\beta$ -TaON with a porous morphology can be synthesized at  $p_{\text{O}_2} = 0.25 \text{ L h}^{-1}$ . This porous structure is particularly advantageous for the enhanced adsorption of reactants and intermediates, enhancing the efficiency of photocatalytic reactions.

Fig. 3 shows the bright-field TEM and HRTEM images and their power spectra (obtained from the part of a single crystal) of the  $\text{Ta}_2\text{O}_5$  and 0.25-O2 and 0-O2 samples synthesized at  $p_{\text{O}_2} = 0.25$  and 0  $\text{L h}^{-1}$ , respectively. The TEM image of  $\text{Ta}_2\text{O}_5$  (Fig. 3a) reveals loosely agglomerated nanoparticles with irregular morphologies and the presence of some poorly crystal-

line particles. In Fig. 3b, the TEM image of the 0.25-O2 sample shows highly agglomerated  $\beta$ -TaON particles, suggesting a compact and porous structure. The elongated particles exhibit well-defined boundaries with relatively higher electron contrast. The TEM image of the 0-O2 sample (Fig. 3c) shows clustered nanostructures of  $\text{Ta}_3\text{N}_5$ , characterized by a dense appearance and irregular round shapes. Although its morphology is somewhat similar to that of  $\text{Ta}_2\text{O}_5$ , the 0-O2 sample features more defined particle edges and porosity. The HRTEM image of  $\text{Ta}_2\text{O}_5$  (Fig. 3a) shows well-defined lattice fringes uniformly extending across the entire particle, indicating a high degree of crystallinity. The observed lattice spacing of 0.39 nm corresponds to the (100) crystallographic plane, consistent with orthorhombic  $\text{Ta}_2\text{O}_5$ . The clear contrast and alignment of the lattice fringes suggest that the particle is either single-crystalline or composed of large crystalline domains. In the case of the 0.25-O2 sample (Fig. 3b), highly ordered lattice fringes with continuous periodicity are observed, which is characteristic of a single crystalline structure with minimal defects (*e.g.*, a stacking fault). The lattice spacing of 0.49 nm corresponds to the (100) crystallographic plane of  $\beta$ -TaON, and the lattice fringe orientation indicates anisotropic growth along specific crystallographic directions. The HRTEM image of the 0-O2 sample shows moderately crystalline domains with visible lattice fringes of 0.35 nm, which can be indexed to the (110) crystallographic plane of orthorhombic  $\text{Ta}_3\text{N}_5$  (Fig. 3c). The corresponding power spectrum of  $\text{Ta}_2\text{O}_5$  shows a well-ordered atomic arrangement perpendicular to the (100) plane (Fig. 3a). The power spectrum of the 0.25-O2 sample exhibits sharp and symmetric diffraction spots aligned along the [100] zone axis, confirming the well-ordered, single-

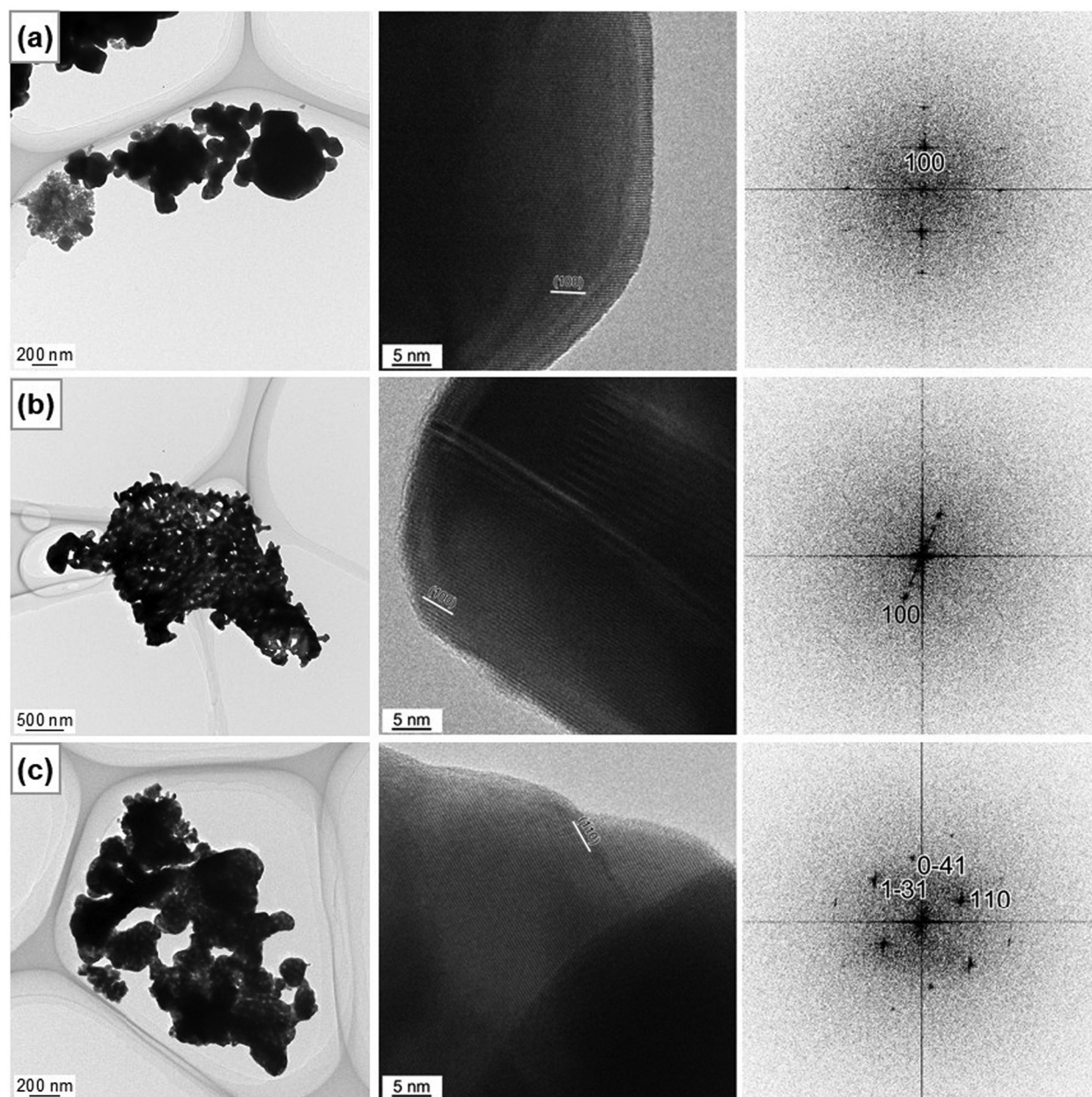


**Fig. 3** Bright-field TEM and HRTEM images and corresponding power spectra of the as-received Ta<sub>2</sub>O<sub>5</sub> (a) and 0.25-O<sub>2</sub> (b) and 0-O<sub>2</sub> (c) samples synthesized under oxygen partial pressures ( $p_{O_2}$ ) of 0.25 and 0 L h<sup>-1</sup>, respectively.

crystalline nature of the observed crystal of orthorhombic Ta<sub>2</sub>O<sub>5</sub> (Fig. 3b). The regular pattern of diffraction spots reflects long-range periodicity and low defect density within the crystal lattice. The power spectrum of the 0-O<sub>2</sub> sample exhibits similarly well-defined and symmetric diffraction spots, characteristic of a single crystal of monoclinic  $\beta$ -TaON. The orientation suggests preferential growth along certain crystallographic directions, and the sharpness and symmetry of the diffraction spots further confirm the high crystallinity and phase purity of synthesized  $\beta$ -TaON. The power spectrum of the 0-O<sub>2</sub> sample reveals a complex pattern of discrete diffraction spots corresponding to orthorhombic Ta<sub>3</sub>N<sub>5</sub>. The indexed maxima of

intensity correspond to reflections from orthorhombic Ta<sub>3</sub>N<sub>5</sub>, including the (110), ( $\bar{1}\bar{3}1$ ), and (041) crystallographic planes (Fig. 3c). This indicates a high degree of crystallinity within the observed domain. However, compared to  $\beta$ -TaON, some irregularities in the diffraction spots indicate the presence of local strain or structural disorder.

Fig. 4 shows the UV-Vis diffuse reflectance spectra and Tauc plots of the as-received Ta<sub>2</sub>O<sub>5</sub> and 0.35-O<sub>2</sub>, 0.25-O<sub>2</sub>, 0.15-O<sub>2</sub>, 0.05-O<sub>2</sub>, and 0-O<sub>2</sub> samples synthesized under varying oxygen partial pressures ( $p_{O_2}$ ) of 0.35, 0.25, 0.15, 0.05, and 0 L h<sup>-1</sup>, respectively. The as-received Ta<sub>2</sub>O<sub>5</sub> sample exhibits minimal absorption in the visible region, with a sharp absorption edge



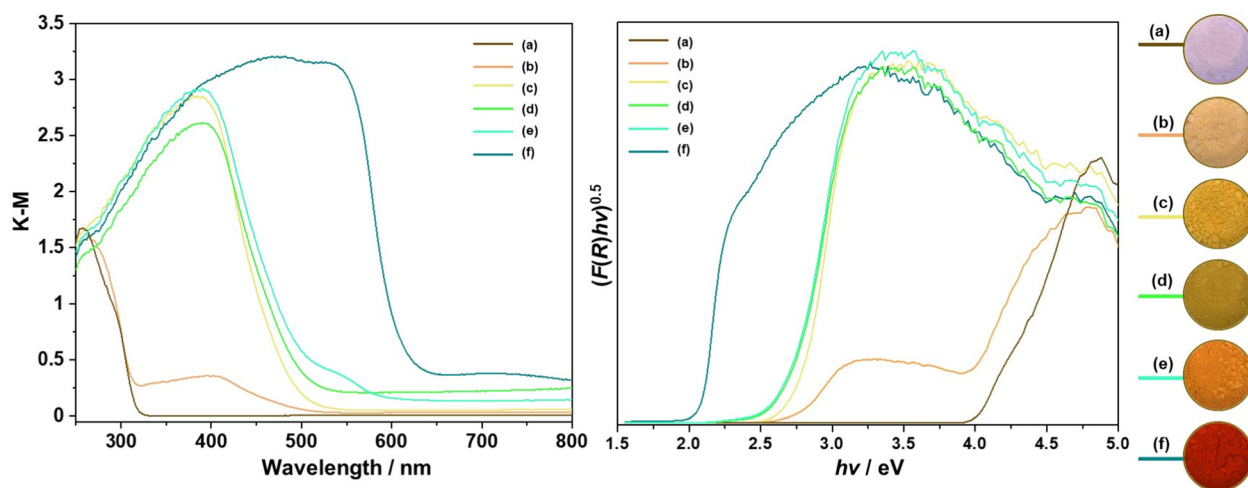


Fig. 4 UV-Vis diffuse reflectance spectra (left) and Tauc plots (right) of the as-received Ta<sub>2</sub>O<sub>5</sub> (a) and 0.35-O<sub>2</sub> (b), 0.25-O<sub>2</sub> (c), 0.15-O<sub>2</sub> (d), 0.05-O<sub>2</sub> (e), and 0-O<sub>2</sub> (f) samples synthesized under oxygen partial pressures ( $p_{O_2}$ ) of 0.35, 0.25, 0.15, 0.05, and 0 L h<sup>-1</sup>, respectively.

located in the deep UV (<320 nm), consistent with its wide band gap of 4.0 eV. A progressive increase in visible light absorption and a clear red-shift of the absorption edge are observed for the samples synthesized by reducing the  $p_{O_2}$  from 0.35 to 0.05 L h<sup>-1</sup>. This is attributed to the introduction of N 2p states, which lie at a higher energy than O 2p states, raising the valence band maximum and reducing the optical band gap in the following order: 4.0 eV (and 2.64 eV) for 0.35-O<sub>2</sub> > 3.85 eV (and 2.75 eV) for 0.25-O<sub>2</sub> > 2.71 eV for 0.15-O<sub>2</sub> = 2.71 eV for 0.05-O<sub>2</sub> > 2.09 eV for 0-O<sub>2</sub>. Notably, the 0-O<sub>2</sub> sample composed of Ta<sub>3</sub>N<sub>5</sub> shows the most pronounced absorption across the UV-Vis range. The background absorption beyond the absorption edge wavelength can be noticed in the UV-Vis diffuse reflectance spectra of the 0.15-O<sub>2</sub>, 0.05-O<sub>2</sub>, and 0-O<sub>2</sub> samples. This is generally attributed to the presence of defects associated with the reduced tantalum species and anion deficiency.<sup>18,45,46</sup> The reduction in  $p_{O_2}$  during synthesis leads to the change in powder colors. The as-received Ta<sub>2</sub>O<sub>5</sub> and 0.35-O<sub>2</sub>, 0.25-O<sub>2</sub>, 0.15-O<sub>2</sub>, 0.05-O<sub>2</sub>, and 0-O<sub>2</sub> samples are white, light beige, yellow ochre, olive yellow, orange ochre, and deep red, respectively. This underlying change in powder color reflects the gradual phase transformation, narrowing of the optical band gap, and the formation of defect states.

Fig. 5a shows the high-resolution Ta 4f XPS spectrum of the as-received Ta<sub>2</sub>O<sub>5</sub>. Deconvolution was performed using a Gaussian fitting model, with the shaded areas representing the fitted envelopes of the spin-orbit doublet. The XPS spectrum exhibits two prominent peaks corresponding to the Ta 4f<sub>5/2</sub> and Ta 4f<sub>7/2</sub> spin-orbit components, centered at approximately 28.04 eV and 26.17 eV, respectively. The observed energy separation of 1.9 eV between these two peaks is characteristic of the Ta<sup>5+</sup> oxidation state and is consistent with previously reported values (1.9 eV).<sup>47</sup> The high symmetry and narrow peak widths suggest a uniform oxidation environment for Ta within the oxide lattice. In Fig. 5d, the Ta 4f XPS spectrum of 0.25-O<sub>2</sub> sample exhibits two deconvoluted peaks cen-

tered at 27.6 eV and 25.7 eV, corresponding to the Ta 4f<sub>5/2</sub> and Ta 4f<sub>7/2</sub> spin-orbit components of  $\beta$ -TaON, respectively. In Fig. 5g, the Ta 4f XPS spectrum of the 0-O<sub>2</sub> sample reveals two distinct peaks at 26.2 eV and 24.3 eV, corresponding to the Ta 4f<sub>5/2</sub> and Ta 4f<sub>7/2</sub> spin-orbit components of Ta<sub>3</sub>N<sub>5</sub>, respectively. As can be noted, these peaks are slightly shifted to the lower binding energies compared to those observed in Ta<sub>2</sub>O<sub>5</sub>. This shift is primarily attributed to the difference in electronegativity between oxygen and nitrogen, with nitrogen being less electronegative. Consequently, the substitution of oxygen with nitrogen increases the electron density around the Ta atoms, resulting in a reduction in the binding energy of the Ta 4f electrons.<sup>48</sup> The N 1s XPS spectrum of the as-received Ta<sub>2</sub>O<sub>5</sub> (Fig. 5b) does not show any peak attributed to N 1s, indicating the absence of nitrogen. Additionally, a weak peak at ~404.5 eV corresponds to the Ta 4p<sub>3/2</sub> core level. The N 1s XPS spectrum of the 0.25-O<sub>2</sub> sample, shown in Fig. 5e, indicates two distinct peaks centered at 396.2 eV and 399.4 eV. These peaks are assigned to Ta-N bonds and O-Ta-N bonding environments in  $\beta$ -TaON, respectively.<sup>49</sup> A broader peak observed at 406.8 eV is attributed to the Ta 4p<sub>3/2</sub> core level. In the N 1s XPS spectrum of the 0-O<sub>2</sub> sample (Fig. 5h), a sharp peak centered at 396.6 eV is observed, which is assigned to the N 1s signal of Ta-N bonds in Ta<sub>3</sub>N<sub>5</sub>, confirming the successful incorporation of nitrogen. Fig. 5c presents the O 1s XPS spectrum of the as-received Ta<sub>2</sub>O<sub>5</sub>.

Upon deconvolution, three distinct peaks are identified. The main peak at ~530.1 eV is attributed to lattice oxygen (Ta-O bonds), confirming the presence of Ta<sub>2</sub>O<sub>5</sub>. A secondary peak centered at ~531.5 eV is associated with oxygen in the oxygen-deficient structure of the lattice and surface-adsorbed oxygen species or hydroxyl groups (-OH), commonly found on the surface of metal oxides/oxynitrides exposed to ambient air. A third, minor peak at ~532.7 eV is assigned to physisorbed water on the surface. Similarly, the O 1s XPS spectrum of 0.25-O<sub>2</sub> sample in Fig. 5f is deconvoluted into three components

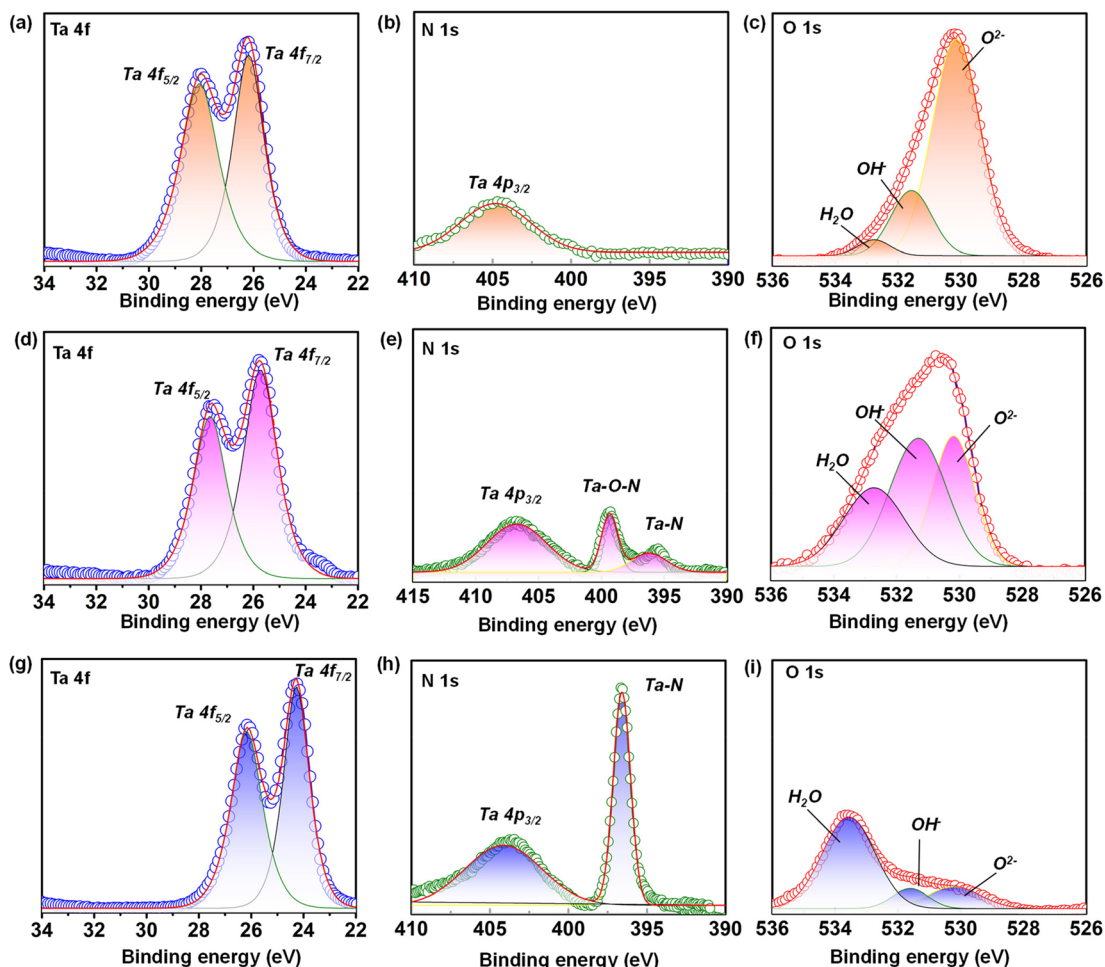


Fig. 5 Ta 4f (left), N 1s (middle), and O 1s (right) XPS spectra of the as-received  $\text{Ta}_2\text{O}_5$  (a–c) and 0.25-O2 (d–f) and 0-O2 (g–i) samples synthesized under oxygen partial pressures ( $p_{\text{O}_2}$ ) of 0.25 and 0  $\text{L h}^{-1}$ , respectively.

centered at 530.2 eV, 531.3 eV, and 532.7 eV, which are also associated with lattice oxygen (Ta–O), oxygen in highly defective regions/surface hydroxyl groups, and adsorbed water molecules, respectively. The intensity of the lattice oxygen peak centered at 530.2 eV in 0.25-O2 sample is slightly reduced compared to that of  $\text{Ta}_2\text{O}_5$  due to the partial substitution of oxygen with nitrogen. The O 1s XPS spectrum of 0-O2 sample (Fig. 5i) is deconvoluted into three components centered at 530.2 eV, 531.6 eV, and 533.6 eV, corresponding to lattice oxygen (Ta–O), oxygen in highly defective regions/surface hydroxyl groups, and physisorbed water, respectively. Notably, the intensities of the Ta–O and –OH related peaks at 530.2 eV and 531.6 eV are significantly reduced compared to those in  $\text{Ta}_2\text{O}_5$ . This trend is consistent with reported data, given that oxygen should be largely absent or present only in minor surface-related forms in  $\text{Ta}_3\text{N}_5$ .<sup>50</sup>

Further, this study also adopts a more sophisticated computational framework by integrating SCAN and HSE06 functionals, in contrast to earlier works relying on the generalized gradient approximation (GGA) or DFT + U methods,<sup>31,38</sup> to more accurately predict structural, electronic, and optical pro-

perties. Fig. 6 shows the total density of states (TDOS) plots for  $\text{Ta}_2\text{O}_5$ ,  $\beta\text{-TaON}$ , and  $\text{Ta}_3\text{N}_5$ , indicating the dependence of the number of electronic states per unit energy as a function of electronic energy. From these TDOS plots, the band gaps of  $\text{Ta}_2\text{O}_5$ ,  $\beta\text{-TaON}$ , and  $\text{Ta}_3\text{N}_5$  are determined to be 4.49 eV, 3.10 eV, and 2.31 eV, respectively, which is consistent with the progressive narrowing of the band gap upon nitrogen incorporation. The TDOS plots also reveal that nitrogen incorporation in  $\text{Ta}_2\text{O}_5$  reduces the density of available electronic states across all energy levels. However, in the case of  $\text{Ta}_3\text{N}_5$ , this trend reverses, with a substantial increase in the density of states, indicating a greater availability of electronic states for transitions, which can have significant implications for optoelectronic properties. Furthermore, the TDOS plots are used to interpret electronic and optical properties, such as absorption, emission, and extinction, by providing insight into the distribution of states accessible for excitation. According to the results of spin-polarized calculations,  $\beta\text{-TaON}$  (Fig. 7b) and  $\text{Ta}_3\text{N}_5$  (Fig. 7c) have symmetric spin-up and spin-down electron densities, confirming their non-magnetic nature. In contrast,  $\text{Ta}_2\text{O}_5$  exhibits spin asymmetry in its TDOS plot (Fig. 7a) and



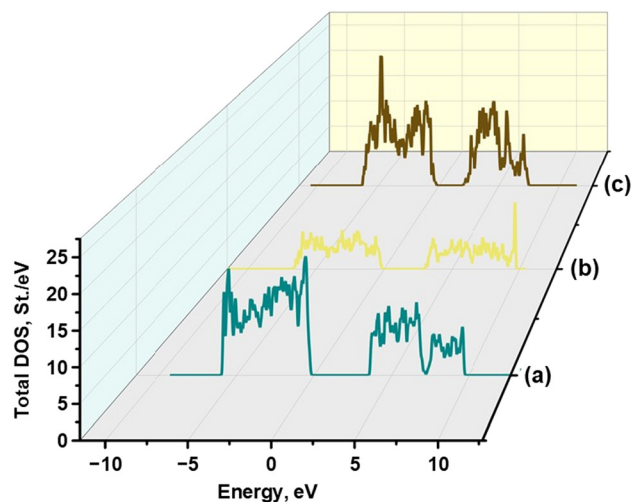


Fig. 6 Total density of states (TDOS) plots of  $\text{Ta}_2\text{O}_5$  (a),  $\beta\text{-TaON}$  (b), and  $\text{Ta}_3\text{N}_5$  (c).

distinct differences in energy gap widths, suggesting subtle magnetic or structural features not observed in its nitrogen-incorporated counterparts. These observations are corroborated by the integral density of states shown in Fig. 7d.

Fig. 8 shows the calculated band edge positions of the conduction and valence bands for  $\text{Ta}_2\text{O}_5$ ,  $\beta\text{-TaON}$ , and  $\text{Ta}_3\text{N}_5$ , with the Fermi level indicated by dashed lines. A clear shift of the

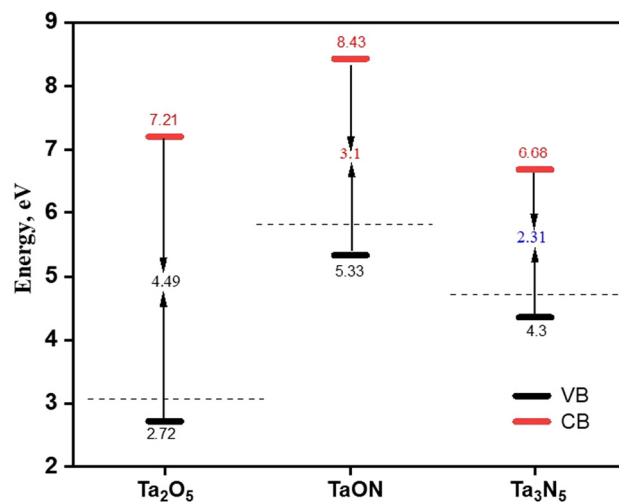


Fig. 8 Calculated band edge positions of the conduction and valence bands for  $\text{Ta}_2\text{O}_5$ ,  $\beta\text{-TaON}$ , and  $\text{Ta}_3\text{N}_5$ . The Fermi level is indicated by dashed lines.

Fermi level toward the conduction band occurs from  $\text{Ta}_2\text{O}_5$  to  $\beta\text{-TaON}$ , followed by a downward shift in  $\text{Ta}_3\text{N}_5$ , reflecting changes in electronic structure and carrier dynamics with increasing nitrogen content. Simultaneously, an increase is observed in key optical parameters, such as the refractive index, dielectric function, and reflection coefficient, as nitro-

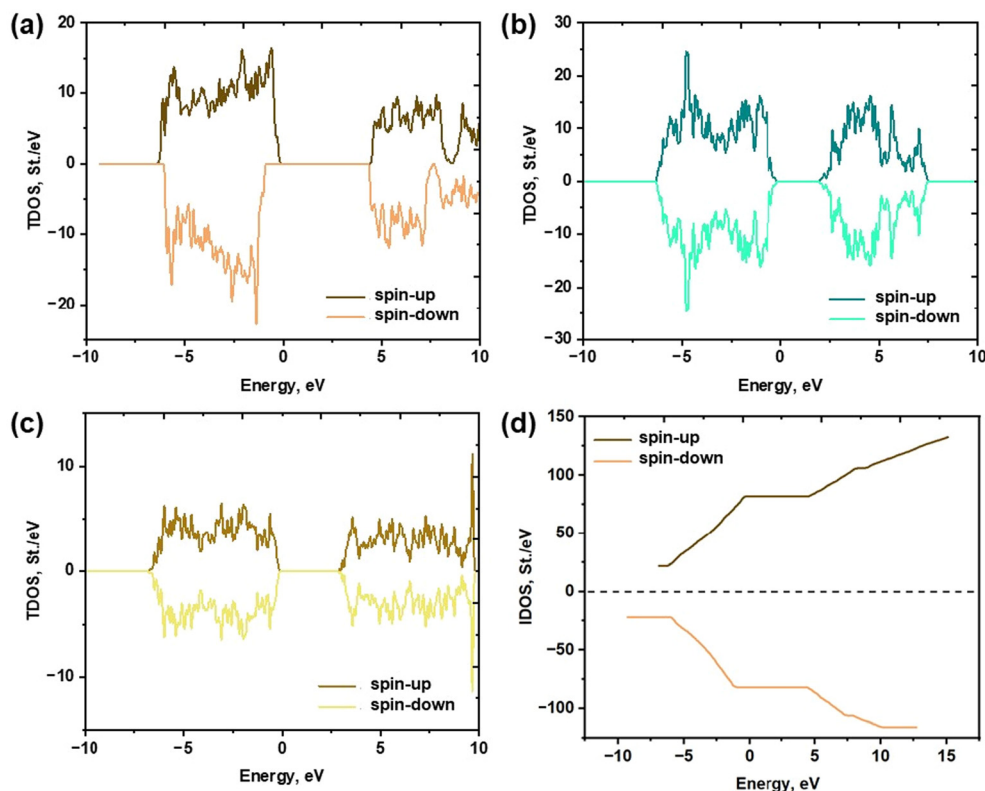


Fig. 7 Spin-resolved total density of states (TDOS) plots of  $\text{Ta}_2\text{O}_5$  (a),  $\beta\text{-TaON}$  (b), and  $\text{Ta}_3\text{N}_5$  (c) and integral density of states (d).

gen content rises (Fig. S1†). The computed values for the refractive index are 2.37, 3.00, and 3.34 for  $\text{Ta}_2\text{O}_5$ ,  $\beta\text{-TaON}$ , and  $\text{Ta}_3\text{N}_5$ , respectively. Their corresponding dielectric constants are 5.76, 7.46, and 10.42, and the calculated values of the reflection coefficient vary in the range of 0.16–0.29 (Fig. S1c†). Further results in Fig. S2† show that as the phase transformation from  $\text{Ta}_2\text{O}_5$  to  $\beta\text{-TaON}$  and  $\text{Ta}_3\text{N}_5$  proceeds, the spectral peaks of the extinction coefficient, energy loss function, and absorption coefficient shift towards lower photon energy values, indicating a reliable tendency in band gap reduction. Notably, nitrogen incorporation introduces additional absorption and extinction features in the 2–4 eV range (Fig. S2a and c†), which may enhance their photocatalytic activity by enabling more efficient utilization of visible light. The reduction in band gap energy facilitates improved light harvesting, rendering  $\beta\text{-TaON}$  and  $\text{Ta}_3\text{N}_5$  more effective for visible-light-driven photocatalytic reactions in comparison to  $\text{Ta}_2\text{O}_5$ . The DFT calculations also reveal a reduction in the effective mass of charge carriers (electrons and holes) upon nitrogen incorporation. This suggests enhanced carrier mobility in  $\beta\text{-TaON}$  and  $\text{Ta}_3\text{N}_5$ , which is a critical factor in boosting photocatalytic efficiency. These findings are consistent with previous studies on related materials.<sup>51,52</sup> Unlike the extinction and absorption behavior, energy loss spectra (Fig. S2b†) indicate that  $\text{Ta}_2\text{O}_5$  exhibits higher energy loss at photon energies above 6 eV, whereas  $\beta\text{-TaON}$  and  $\text{Ta}_3\text{N}_5$  show reduced loss,

further supporting their suitability for optoelectronic and photocatalytic applications.

Following the structural and optical characterization, photoelectrochemical (PEC) studies were conducted to evaluate the critical influence of oxygen partial pressure on the phase evolution and their light-driven activity. The tantalum (oxy)nitrides, synthesized under decreasing oxygen partial pressures ( $p_{\text{O}_2} = 0.35, 0.25, 0.15, 0.05$ , and  $0 \text{ L h}^{-1}$ ), exhibited a progressive transformation in composition, as confirmed by XRD: from pure orthorhombic  $\text{Ta}_2\text{O}_5$  in the as-received sample to mixed phases of  $\text{Ta}_2\text{O}_5$  and  $\beta\text{-TaON}$  at  $p_{\text{O}_2} = 0.35 \text{ L h}^{-1}$ , and predominantly  $\beta\text{-TaON}$  at  $p_{\text{O}_2} = 0.25 \text{ L h}^{-1}$ . At lower  $p_{\text{O}_2}$  (0.15 and  $0.05 \text{ L h}^{-1}$ ),  $\beta\text{-TaON}$  coexisted with  $\text{Ta}_3\text{N}_5$  though the latter appeared only in trace amounts at  $0.15 \text{ L h}^{-1}$ . A full conversion to single-phase  $\text{Ta}_3\text{N}_5$  was achieved under nitrogen-only conditions ( $0 \text{ L h}^{-1}$ ), enabling a direct comparison of PEC performance as a function of nitridation degree.

To evaluate the PEC activity of these materials, open circuit potential (OCP) measurements were conducted under different values of irradiance. This method provided a sensitive probe of the photoinduced charge separation capabilities of the photoanodes.<sup>53</sup> As shown in Fig. 9A, all synthesized samples exhibited a logarithmic shift of the OCP toward more negative values upon increasing light intensity, signifying the accumulation of photo-generated electrons in the semiconductor. However, it is worth

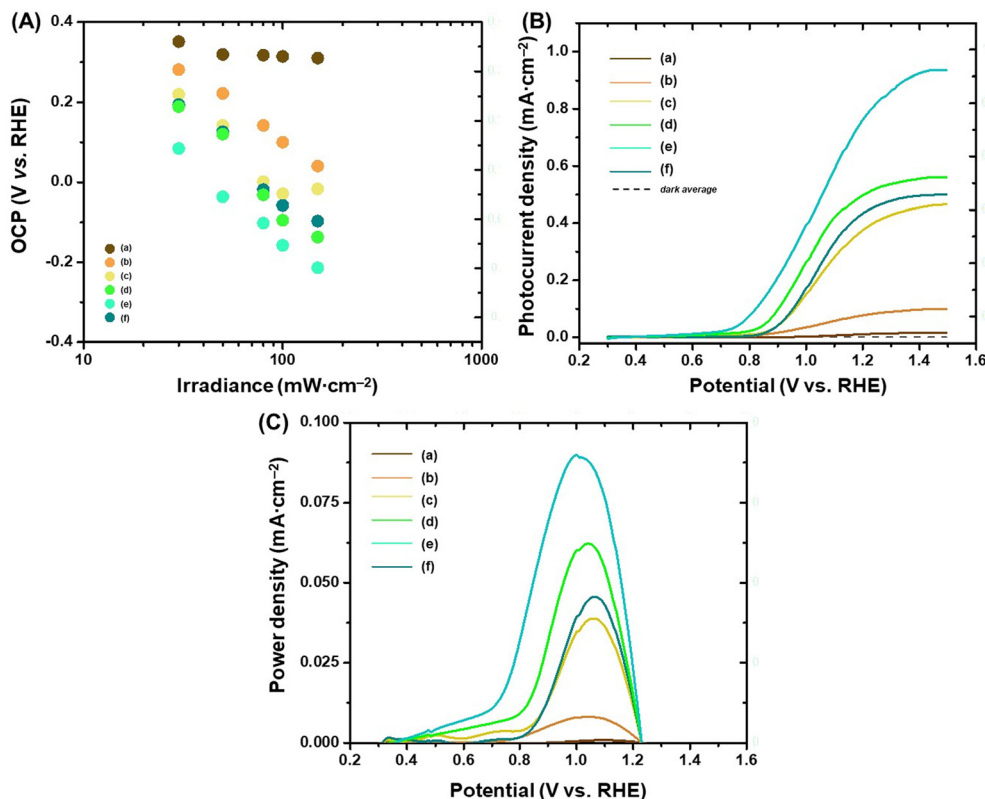


Fig. 9 Plot of OCP vs. irradiance (A), LSV (B), and power density vs. potential (C) of as-received  $\text{Ta}_2\text{O}_5$  (a) and 0.35-O2 (b), 0.25-O2 (c), 0.15-O2 (d), 0.05-O2 (e), and 0-O2 (f).

noting that the as-received Ta<sub>2</sub>O<sub>5</sub> showed a very small and constant change at high irradiance, probably due to the need for absorption of the scarce, very high-energy UV light. In all cases, this negative shift reflects the development of a chemical potential gradient for electrons directly related to the photon absorption rate and carrier dynamics.<sup>54</sup> Notably, larger shifts in OCP under illumination are indicative of efficient charge generation and separation, with concomitantly reduced recombination rates. The magnitude of the OCP shift followed the trend: 0.05-O2 > 0.15-O2 > 0-O2 > 0.25-O2 > 0.35-O2 > as-received Ta<sub>2</sub>O<sub>5</sub> (very small changes), which aligns with the expected PEC response for materials exhibiting solar light absorption and active band alignment. This result confirmed that all modified samples functioned as light-responsive photoanodes, with varying degrees of thermodynamic driving force for surface photoredox reactions under open-circuit conditions.

Linear sweep voltammetry (LSV) under illumination (Fig. 9B) further differentiated the PEC response across the sample series, with the sustained photocurrent at the interface primarily attributed to the water oxidation reaction (WOR).<sup>25,27</sup> At 1.2 V vs. RHE, the photocurrent densities were 0.762, 0.497, 0.434, 0.376, 0.077, and 0.011  $\mu\text{A}\cdot\text{cm}^{-2}$  for the 0.05-O2, 0.15-O2, 0-O2, 0.25-O2, 0.35-O2, and as-received Ta<sub>2</sub>O<sub>5</sub> samples, respectively. This same hierarchy persisted over the entire potential range, again emphasizing the superior charge transfer characteristics of the samples containing both  $\beta$ -TaON and

Ta<sub>3</sub>N<sub>5</sub>. It is again observed that the resolved PEC response of the as-received Ta<sub>2</sub>O<sub>5</sub> is very low, approaching the response in the dark. The need to illuminate with higher-energy UV light limits the PEC response of this material. The corresponding onset potentials for photocurrent generation (defined as the potential at which significant photocurrent began) were 0.77, 0.86, 0.90, 0.91, and 1.00 V vs. RHE, for the 0.05-O2, 0.15-O2, 0-O2, 0.25-O2, and 0.35-O2 samples, respectively. These values suggest a reduction in internal resistances, such as recombination losses, in the samples synthesized at lower oxygen partial pressures, particularly those incorporating both  $\beta$ -TaON and Ta<sub>3</sub>N<sub>5</sub> phases.

Power density *versus* potential plot (Fig. 9C) shows bell-shaped curves with maxima between 1.0 and 1.1 V vs. RHE, and this behavior aligns with that reported for other *n*-type semiconductors.<sup>27,28</sup> Peak power densities were 89, 62, 46, 39, and 8  $\mu\text{W}\cdot\text{cm}^{-2}$  for 0.05-O2, 0.15-O2, 0-O2, 0.25-O2, and 0.35-O2, respectively. The result for the as-received Ta<sub>2</sub>O<sub>5</sub> is quite low that it is impractical for reliable sunlight-activated PEC approaches. These values corroborate that the 0.05-O2 and 0.15-O2 samples were the most effective photoanodes in terms of light-to-chemical energy conversion. Assuming ideal behavior governed by Faraday's law, at 1.0 V vs. RHE, these photoanodes were predicted to sustain hydrogen evolution rates of 2.01  $\mu\text{mol}\cdot\text{cm}^{-2}\cdot\text{s}^{-1}$  and 1.35  $\mu\text{mol}\cdot\text{cm}^{-2}\cdot\text{s}^{-1}$ , respectively, under appropriate dual-electrode PEC conditions.

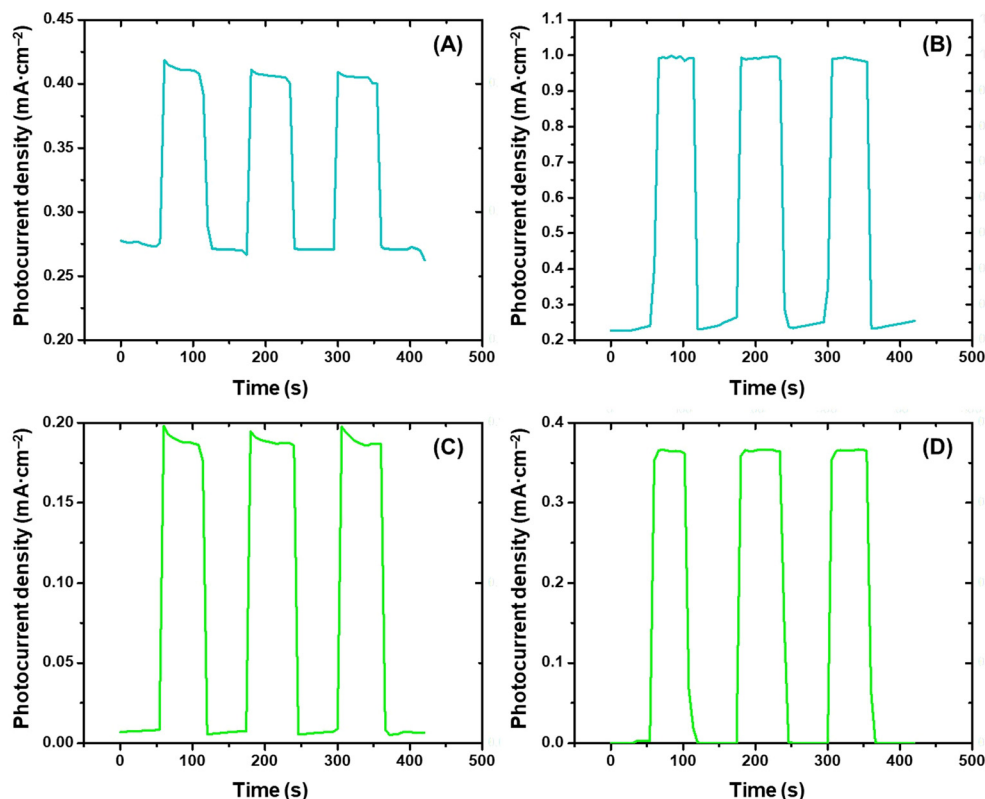


**Fig. 10** CA at 1 V vs. RHE under chopped irradiation of 0.05-O2 (A and B) and 0.15-O2 (C and D) samples: 0.1 M Na<sub>2</sub>SO<sub>4</sub> (A and C) and 0.1 M Na<sub>2</sub>SO<sub>4</sub> + 5 mM potassium ferrocyanide (B and D).



The enhanced PEC performance of the 0.05-O2 and 0.15-O2 samples may be attributed to the formation of interfaces among the  $\beta$ -TaON and  $\text{Ta}_3\text{N}_5$  heterostructures, which could enhance charge separation and transfer due to the favorable band alignments. However, further experimental studies are required to confirm the formation and role of such heterostructures. Based on the DFT-derived electronic band positions,  $\beta$ -TaON possesses a valence band (VB) at 5.33 eV and a conduction band (CB) at 8.43 eV (*vs.* vacuum), while  $\text{Ta}_3\text{N}_5$  features a VB at 4.3 eV and a CB at 6.68 eV. This type-II band alignment would favor the transfer of photo-excited electrons from the CB of  $\beta$ -TaON to that of  $\text{Ta}_3\text{N}_5$ , while holes in the VB of  $\text{Ta}_3\text{N}_5$  could migrate toward the VB of  $\beta$ -TaON. The spatial separation of charge carriers inherent to this configuration would reduce recombination rates and increase photocurrent efficiency.<sup>55</sup> In contrast, the 0.35-O2 sample, containing  $\text{Ta}_2\text{O}_5$  and  $\beta$ -TaON, may also form heterostructures, but the wider bandgap and limited visible absorption of  $\text{Ta}_2\text{O}_5$  likely diminished overall PEC performance.

Despite their superior performance, the best-performing photoanodes (0.05-O2 and 0.15-O2) are expected to degrade over time due to the stability issues of  $\text{Ta}_3\text{N}_5$  under illumination in aqueous media.<sup>56–58</sup> To test the possibility of improving PEC performance, potassium ferrocyanide was employed as a sacrificial electron donor (SED) in the electrolyte. The redox activity of ferrocyanide enables it to donate electrons to photo-generated holes, sustaining interfacial charge transfer, promoting electron flow toward the external circuit, and thereby mitigating the self-oxidation of the photoanode.<sup>58,59</sup> As shown in Fig. 10, chopped CA measurements revealed a substantial increase in photocurrent under illumination in the presence of ferrocyanide. Moreover, transient responses demonstrated reduced overshoot and spike artifacts, which are typically associated with surface recombination and trap states.<sup>60</sup> These features were particularly minimized in the 0.05-O2 sample, suggesting more effective charge separation and faster surface kinetics when ferrocyanide was employed.

The formation of  $\beta$ -TaON/ $\text{Ta}_3\text{N}_5$  composite under optimized ammonolysis conditions provided significant enhancements in the PEC response, both thermodynamically (*via* OCP shift) and kinetically (*via* improvement of photocurrent and power density). The band alignment and phase composition define the PEC behavior, highlighting the synergistic effect of combining solar-light-absorbing and structurally robust materials. Furthermore, the use of ferrocyanide as SED provided a valuable strategy for testing improvements in charge transfer properties while reducing secondary reactions. These findings underscore the promise of tailored oxynitride/nitride heterostructures for solar fuel applications as photoanodes.

## 4. Conclusions

In summary, this study systematically investigated the critical influence of oxygen partial pressure on the phase transformation of tantalum-based materials during ammonolysis. A con-

trolled transformation from  $\text{Ta}_2\text{O}_5$  to  $\beta$ -TaON, and subsequently to  $\text{Ta}_3\text{N}_5$ , was achieved by tuning the oxygen flow rate from 0 to 0.35 L h<sup>-1</sup>. Notably, phase-pure  $\beta$ -TaON was synthesized at an intermediate oxygen flow rate of 0.25 L h<sup>-1</sup>, highlighting the narrow synthesis window and thermodynamic sensitivity of this polymorph. Comprehensive characterizations, complemented by DFT calculations, revealed that nitrogen incorporation reduced the optical band gap, modulated the electronic structure, and lowered the charge carrier effective masses, which collectively enhanced charge separation and transport. Photoelectrochemical (PEC) measurements demonstrated that the selectively formed  $\beta$ -TaON/ $\text{Ta}_3\text{N}_5$  heterostructures exhibited enhanced photocurrent density and power density due to a type-II band alignment that promotes efficient charge carrier separation. The use of a sacrificial electron donor (ferrocyanide) further enhanced PEC performance by facilitating interfacial charge transfer and suppressing recombination. Nevertheless, long-term operational stability remains a challenge, and effective protection strategies need to be further investigated to ensure its robust PEC performance. Overall, this study presents a synthesis approach for tuning the phase composition and optoelectronic properties of tantalum (oxy)nitrides by controlling oxygen partial pressure. The findings provide valuable insights into the synthesis of phase-pure  $\beta$ -TaON and underscore the potential of these materials in solar fuel applications.

## Conflicts of interest

There are no conflicts to declare.

## Data availability

All data supporting the findings of this study are available from the authors on request.

## Acknowledgements

This work was funded by a Novo Nordisk Foundation RECRUIT Grant (NNF23OC0079059). This work was also supported in part by the World Research Hub (WRH) Program of the Institute of Science Tokyo and the “Invitational Fellowship for Research in Japan” Program of the Japan Society for the Promotion of Science (S22063). This work was also supported in part by the Meiji University International Collaborative Research Promotion Project (MU-OSRI-ICRPP2023-206). MH would like to thank Prof. Martin Lerch for providing access to his research laboratory at Technische Universität Berlin, Germany. The authors would like to thank Dipl. Phys. Christoph Fahrenson from ZELMI, TU Berlin, Germany, and Reiko Shiozawa from Shinshu University, Japan, for their technical support in SEM and XPS analyses, respectively. KY was partly supported by the Japan Society for the Promotion of Science (KAKENHI Grant no. JP23K04373) and the Institute for

Materials Research, Tohoku University, Japan (GIMRT Program, proposal no. 202311-RDKGE-0001).

## References

- H. Kageyama, K. Hayashi, K. Maeda, J. P. Attfield, Z. Hiroi, J. M. Rondinelli and K. R. Poeppelmeier, *Nat. Commun.*, 2018, **9**, 772.
- A. Kudo and Y. Miseki, *Chem. Soc. Rev.*, 2009, **38**, 253–278.
- K. Maeda and K. Domen, *J. Phys. Chem. C*, 2007, **111**, 7851–7861.
- S. G. Ebbinghaus, H. P. Abicht, R. Dronskowski, T. Müller, A. Reller and A. Weidenkaff, *Prog. Solid State Chem.*, 2009, **37**, 173–205.
- G. Brauer and J. R. Weidlein, *Angew. Chem.*, 1965, **77**, 913.
- S. Cosgun, *Synthese und Charakterisierung Tantaloxidnitrid-basierter Verbindungen für die photokatalytische Wasserspaltung*, Ph.D. Thesis, Technische Universität Berlin, 2015.
- H. Schilling, A. Stork, E. Irran, H. Wolff, T. Bredow, R. Dronskowski and M. Lerch, *Angew. Chem., Int. Ed.*, 2007, **46**, 2931–2934.
- D. A. Weber, *Synthese und Charakterisierung neuer Oxide und Oxidnitride der Elemente der 5. und 6. Gruppe des Periodensystems*, Ph.D. Thesis, Technische Universität Berlin, 2014.
- T. Lüdtke, D. Weber, A. Schmidt, A. Müller, C. Reimann, N. Becker, T. Bredow, R. Dronskowski, T. Ressler and M. Lerch, *Z. Kristallogr.*, 2017, **232**, 3–14.
- D. Armytage and B. E. F. Fender, *Acta Crystallogr., Sect. B*, 1974, **30**, 809–812.
- T. Lüdtke, A. Schmidt, C. Göbel, A. Fischer, N. Becker, C. Reimann, T. Bredow, R. Dronskowski and M. Lerch, *Inorg. Chem.*, 2014, **53**, 11691–11698.
- H. Schilling, M. Lerch, A. Börger, K. D. Becker, H. Wolff, R. Dronskowski, T. Bredow, M. Tovar and C. Baetz, *J. Solid State Chem.*, 2006, **179**, 2416–2425.
- A. Stork, H. Schilling, C. Wessel, H. Wolff, A. Börger, C. Baetz, K. D. Becker, R. Dronskowski and M. Lerch, *J. Solid State Chem.*, 2010, **183**, 2051–2058.
- Y. A. Buslaev, G. M. Safronov, V. I. Pakhomov, M. A. Glushkova, V. P. Repko, M. M. Ershova, A. N. Zhukov and T. A. Zhdanova, *Izv. Akad. Nauk SSSR, Neorg. Mater.*, 1969, **5**, 45–48.
- M. W. Lumey and R. Dronskowski, *Z. Anorg. Allg. Chem.*, 2003, **629**, 2173–2179.
- K. Woodhead, S. Pascarelli, A. L. Hector, R. Briggs, N. Alderman and P. F. McMillan, *Dalton Trans.*, 2014, **43**, 9647–9654.
- M. Hara, G. Hitoki, T. Takata, J. N. Kondo, H. Kobayashi and K. Domen, *Catal. Today*, 2003, **78**, 555–560.
- M. Hojamberdiev, H. Wagata, K. Yubuta, K. Kawashima, J. J. M. Vequizo, A. Yamakata, S. Oishi, K. Domen and K. Teshima, *Appl. Catal., B*, 2016, **182**, 626–635.
- M. Hojamberdiev and I. Gonzalo-Juan, *J. Ceram. Soc. Jpn.*, 2016, **124**, 1052–1055.
- E. Orhan, F. Tessier and R. Marchand, *Solid State Sci.*, 2002, **4**, 1071–1076.
- M. Rohloff, S. Cosgun, C. Massué, T. Lunkenbein, A. Senyshyn, M. Lerch, A. Fischer and M. Behrens, *Z. Naturforsch., B*, 2019, **74**, 71–83.
- J. C. McGlynn, M. D. Cappelluti, J. M. Hanlon, S. Saremi-Yarahmadi, N. Flores-González and D. H. Gregory, *Solid State Sci.*, 2024, **148**, 107410.
- S. Yoon, A. E. Maegli, S. K. Matam, M. Trottmann, T. Hisatomi, C. M. Leroy, M. Grätzel, S. Pokrant and A. Weidenkaff, *Int. J. Photoenergy*, 2013, **2013**, 507194.
- M. Kodera and K. Sayama, *ChemCatChem*, 2022, **14**, e202201004.
- M. Hojamberdiev, J. M. Mora-Hernandez, R. Vargas, A. Yamakata, K. Yubuta, E. M. Heppke, L. M. Torres-Martínez, K. Teshima and M. Lerch, *ACS Appl. Energy Mater.*, 2021, **4**, 9315–9327.
- L. S. Gómez Velázquez, M. L. Dell'Arciprete, L. Madriz and M. C. Gonzalez, *Catal. Commun.*, 2023, **175**, 106617.
- L. Madriz, J. Tatá, D. Carvajal, O. Núñez, B. R. Scharifker, J. Mostany, C. Borrás, F. M. Cabrerizo and R. Vargas, *Renewable Energy*, 2020, **152**, 974–983.
- R. Vargas, D. Méndez, D. Torres, D. Carvajal, F. M. Cabrerizo and L. Madriz, *Int. J. Hydrogen Energy*, 2024, **59**, 159–167.
- G. Kresse and J. Furthmüller, *Comput. Mater. Sci.*, 1996, **6**, 15–50.
- M. A. Lahmer, *Comp. Condens. Matter*, 2023, **36**, e00824.
- P. Li, W. Fan, Y. Li, H. Sun, X. Cheng, X. Zhao and M. Jiang, *Inorg. Chem.*, 2010, **49**, 6917–6924.
- J. Sun, A. Ruzsinszky and J. P. Perdew, *Phys. Rev. Lett.*, 2015, **115**, 036402.
- P. Deák, B. Aradi, T. Frauenheim, E. Janzén and A. Gali, *Phys. Rev. B: Condens. Matter Mater. Phys.*, 2010, **81**, 153203.
- Y. Duan, L. Qin, L. Shi and G. Tang, *Comput. Mater. Sci.*, 2015, **101**, 56–61.
- V. Barone, O. Hod, J. E. Peralta and G. E. Scuseria, *Acc. Chem. Res.*, 2011, **44**, 269–279.
- M. Yashima, Y. Lee and K. Domen, *Chem. Mater.*, 2007, **19**, 588–593.
- H. Wolff, T. Bredow, M. Lerch, H. Schilling, E. Irran, A. Stork and R. Dronskowski, *J. Phys. Chem. A*, 2007, **111**, 2745–2749.
- E. Nurlaela, M. Harb, S. del Gobbo, M. Vashishta and K. Takanabe, *J. Solid State Chem.*, 2015, **229**, 219–227.
- Q. Zhao, M. Cui and T. Liu, *ChemPhysChem*, 2022, **23**, e202100859.
- J. M. del Campo, J. L. Gázquez, S. B. Trickey and A. Vela, *J. Chem. Phys.*, 2012, **136**, 104108.
- D. Lu, G. Hitoki, E. Katou, J. N. Kondo, M. Hara and K. Domen, *Chem. Mater.*, 2004, **16**, 1603–1605.
- A. E. Maegli, S. Pokrant, T. Hisatomi, M. Trottmann, K. Domen and A. Weidenkaff, *J. Phys. Chem. C*, 2014, **118**, 16344–16351.

- 43 M. Hojamberdiev, M. F. Bekheet, E. Zahedi, H. Wagata, J. J. M. Vequizo, A. Yamakata, K. Yubuta, A. Gurlo, K. Domen and K. Teshima, *Dalton Trans.*, 2016, **45**, 12559–12568.
- 44 M. Hojamberdiev, K. Kawashima, T. Hisatomi, M. Katayama, M. Hasegawa, K. Domen and K. Teshima, *Faraday Discuss.*, 2019, **215**, 227–241.
- 45 A. Kasahara, K. Nukumizu, T. Takata, J. N. Kondo, M. Hara, H. Kobayashi and K. Domen, *J. Phys. Chem. B*, 2003, **107**, 791–797.
- 46 M. Hojamberdiev, E. Zahedi, E. Nurlaela, K. Kawashima, K. Yubuta, M. Nakayama, H. Wagata, T. Minegishi, K. Domen and K. Teshima, *J. Mater. Chem. A*, 2016, **4**, 12807–12817.
- 47 E. Atanassova and D. Spassov, *Appl. Surf. Sci.*, 1998, **135**, 71–82.
- 48 Y. Dong, F. Ai, D. Sun-Waterhouse, K.-I. Murai, T. Moriga and G. I. N. Waterhouse, *Chem. Mater.*, 2023, **35**, 8281–8300.
- 49 H. Jiang, Y. Shi and S. Zang, *Int. J. Hydrogen Energy*, 2023, **48**, 17827–17837.
- 50 W. J. Chun, A. Ishikawa, H. Fujisawa, T. Takata, J. N. Kondo, M. Hara, M. Kawai, Y. Matsumoto and K. Domen, *J. Phys. Chem. B*, 2003, **107**, 1798–1803.
- 51 X. Ma, Y. Dai, M. Guo and B. Huang, *ChemPhysChem*, 2012, **13**, 2304–2309.
- 52 Y. Zhang, J. Liu, Y. S. Kang and X. L. Zhang, *Nanoscale*, 2022, **14**, 11909–11922.
- 53 F. E. Bedoya-Lora, I. Holmes-Gentle and A. Hankin, *Curr. Opin. Green Sustainable Chem.*, 2021, **29**, 100463.
- 54 X. Li and S. Pan, *Adv. Sensor Energy Mater.*, 2023, **2**, 100057.
- 55 J. Low, J. Yu, M. Jaroniec, S. Wageh and A. A. Al-Ghamdi, *Adv. Mater.*, 2017, **29**, 1601694.
- 56 K. Seki, T. Higashi, Y. Kawase, K. Takanabe and K. Domen, *J. Phys. Chem. Lett.*, 2022, **13**, 10356–10363.
- 57 S. Y. Chae and E. D. Park, *Appl. Surf. Sci.*, 2022, **583**, 152566.
- 58 S. Khan, M. J. Leite Santos, J. Dupont and S. R. Teixeira, *IOP Conf. Ser.:Mater. Sci. Eng.*, 2015, **97**, 012007.
- 59 Y. He, R. Chen, W. Fa, B. Zhang and D. Wang, *J. Chem. Phys.*, 2019, **151**, 130902.
- 60 L. M. Peter, A. B. Walker, T. Bein, A. G. Hufnagel and I. Kondofersky, *J. Electroanal. Chem.*, 2020, **872**, 114234.